Electronic Supporting Information

Topological and Network Analysis of Lithium Ion Battery Components: The Importance of Pore Space Connectivity for Cell Operation

Marie Francine Lagadec, Raphael Zahn, Simon Müller, and Vanessa Wood*

Department of Information Technology and Electrical Engineering, ETH Zurich, Zurich CH-8092, Switzerland

* To whom correspondence should be addressed. E-mail: vwood@ethz.ch

1. Effective transport properties of the Celgard® PP1615 separator

The Celgard® PP1615 separator was analysed as described in our previous work[1]. This separator has relatively large pore channels leading to a large representative volume element (RVE) with an edge length of ~3 µm (see **Figure S1a**). For the Targray PE16A separator dataset[2], the RVE edge length is ~2 µm as determined in our previous work[1]. For the PP RVE edge length of 3 µm, we determine a porosity ε of 40.19±1.03 % (**Figure S1b**), tortuosities τ_{TP} = 2.04±0.19, τ_{IP1} = 2.31±0.24, and τ_{IP2} = 24.89±6.15 (**Figure S1c**). This is also reflected in the effective transport coefficients δ_{TP} = 19.9±2.0 %, δ_{IP1} 17.6±2.1 %, and δ_{IP2} = 1.7±0.4 % (**Figure S1d**); effective transport in the IP2 direction is thus approximately ten times worse than in the TP or IP1 directions.

The pore networks of both the Targray PE16A and the Celgard® PP1615 separators consist of a single interconnected pore network. Small areas of non-connected pore space that might be present in these separators do not contribute to ionic transport across the separator and should be omitted for performance evaluations. Our imaging process relies on infilling the connected pore structure of the separator with material of a high imaging contrast[1]. This infilling process omits the non-connected pore space yielding a single interconnected pore network.

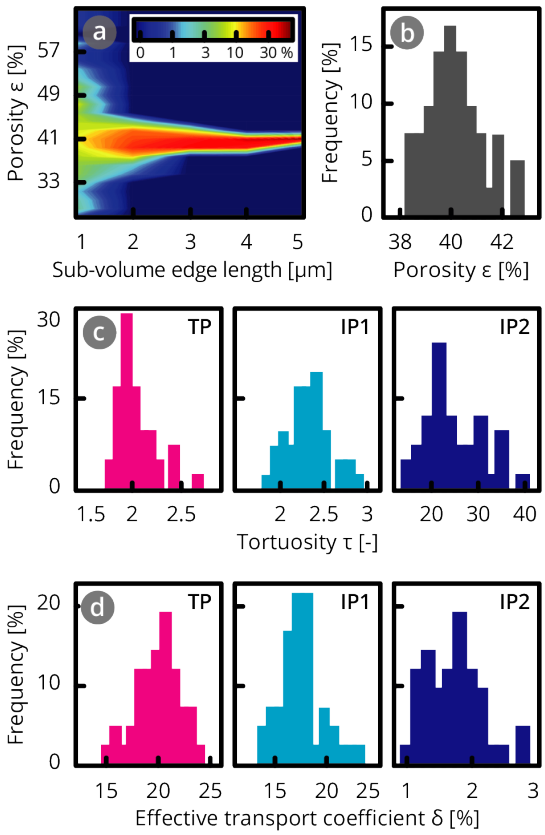

Figure S1. (a) Scale space analysis of the Celgard® PP1615 dataset[3] showing the convergence of the porosity distributions at different sub-volume sizes towards the mean value. (b) Porosity ε, (c) tortuosity τ, and (d) effective transport coefficient δ histograms for TP, IP1, and IP2 directions of the 3 µm edge length sub-volumes.

2. Extensive and intensive Minkowski functionals

The pore space of a binary structure is defined as P, which has an embedding space Ω (P $\subset$ Ω, with Ω occupying the total dataset volume, V_Ω). The pore space's boundary is δP, and its surface element for cylindrically-shaped structures is ds = R dz dϕ. The *extensive* Minkowski functionals, $M_x(P)$ (with x $\in$ {0, …, d} and d being the dimensionality of the structure of interest, here: d = 3), can also be expressed as *intensive* parameters (i.e., normalised functionals), $m_x(P)$.[4]

$$m_x(\mathrm{P}) = \frac{M_x(\mathrm{P} \cap \Omega)}{\mathrm{V}_\Omega}$$

The first Minkowski functional, $M_0(P)$, corresponds to the pore volume, V_{Pore}:

$$\mathrm{M}_0(\mathrm{P}) = \mathrm{V}_{\mathrm{Pore}}(\mathrm{P}).$$

The first normalised Minkowski functional, $m_0(P)$, corresponds to a structure's porosity, ε. For N non-intersecting cylindrical pores of height h and radius R (see **Figure 2a** in the main text), $M_0(P)$ becomes N • π R^2 • h.

The second Minkowski functional, $M_1(P)$, measures the interfacial area between pores and solid phase. The corresponding normalised functional is the specific surface area, $m_1(P)$.

$$M_1(P) = \int_{\delta P} ds$$

For N non-intersecting cylindrical pores of height h and radius R (**Figure 2a**), the integral yields N • 2 π R • (R + h).

The third Minkowski functional, $M_2(P)$, measures the mean curvature, H(P), over the interface and is a one-dimensional shape factor for 3D shapes. The corresponding normalised functional is called mean breadth density, $m_2(P)$.

$$M_2(P) = \frac{1}{2\pi}\int_{\delta P} H(P)\, ds = \frac{1}{4\pi}\int_{\delta P}\left[\frac{1}{r_{min}} + \frac{1}{r_{max}}\right] ds$$

For N non-intersecting cylindrical pores of height h and radius R (**Figures 2a** and **3a**) the integral yields N/2 • (h + π • R). Thus, for long, small pores, $M_2(P)$ becomes N•h/2. For complex structures with interconnectivity in several directions (**Figures 3b-c**), $M_2(P)$ becomes more complex, and can be calculated numerically, but no longer analytically.

The fourth Minkowski functional, $M_3(P)$, measures the Gaussian curvature, K(P), over the interface (thus, the total curvature), and is proportional to the Euler-Poincaré characteristic, X(P), a topological invariant.

$$M_3(P) = \int_{\delta P} K(P)\, ds = \int_{\delta P}\left[\frac{1}{r_{min} \cdot r_{max}}\right] ds = \\ = 4\pi \cdot X$$

In 3D, the characteristic X is linked to the Betti numbers β_0 (number of objects N), β_1 (connectivity C) and β_2 (number of enclosed cavities), and, for a voxel-based dataset, to N_V (number of vertices), N_E (number of edges), N_F (number of faces), and N_{vox} (number of voxels, or solids).[4,5]

$$X = \beta_0 - \beta_1 + \beta_2 = N_V - N_E + N_F - N_{vox}$$

For percolating networks of pores and solid (i.e., without enclosed cavities), the characteristic X of the pore space can simply be expressed by the number of pores, N (N $\geqq$ 0), and the connectivity, C (C $\geqq$ 0).

$$X = N - C$$

The corresponding normalised parameters, χ and c, are the Euler-Poincaré characteristic density and the connectivity density.

3. Minkowski functionals of separator microstructures

Minkowski functionals have previously been linked to transport related parameters. The shape factor, in combination with the surface area, provides a first approximation of the diffusion coefficient[6]. Structures with high connectivity have large node and branch densities, and higher order nodes are associated with more spreading power.[7] Meanwhile, in diffusion simulations, branches that dead-end do not contribute to effective transport through the structure.[8]

The intensive Minkowski functionals (i.e., normalised to the analysed volume and designated here with m_x) are listed in **Table T1**. As designed, the reference separator microstructures replicate porosities well within the specified porosity of 40±2 and 40±5 % of the PE and PP separators. The specific surface area of the reference datasets slightly decreases as more pores are added in a second and third perpendicular direction. The specific surface area (m_1) of the PE separator (11.72 μm^{-1}) is almost identical to m_1 of artificially generated microstructures with pores in three perpendicular directions (11.62 μm^{-1}). This is expected since pore size as well as porosity were chosen to match the parameters of the PE separator. It shows that cylindrical pore segments are a good approximation for the pore shape in the PE separator. For the PP separator, the value for m_1 is lower (5.22 μm^{-1}) due to the larger pores in PP.

m_2 can be interpreted as a measure of shape of the surface. For the all structures (reference and real), the values are positive, indicating that the shape of the pore surface is on average convex.[9,10] For the reference datasets with cylindrical pores in one direction, the shape factor scales with the number of pores *N* and with $h+\pi \cdot R$, where *h* is the pore length and *R* is the pore radius. As more pores are introduced in a second and third perpendicular direction,

Table T1. Average values and standard deviations of the intensive Minkowski functionals m_0, m_1, m_2, as well as Euler-Poincaré characteristics and connectivity densities χ and c, respectively, for the artificially generated microstructures (1D, 2D and 3D) and the imaged Targray PE16A (PE) and Celgard® PP1615 (PP) separator microstructures of edge lengths 5 µm each. The values for χ and c are calculated via the Minkowski functional M_3.

Parameter	1D	2D	3D	PE	PP
Porosity m_0 [%]	39.95±0.00	40.48±0.07	41.04±0.04	40.53±0.77	40.19±0.42
Specific surface area m_1 [μm^{-1}]	13.94±0.00	12.11±0.02	11.62±0.02	11.72±0.13	5.22±0.14
Shape factor density m_2 [μm^{-2}]	17.40±0.01	7.82±0.03	5.44±0.03	6.68±0.35	1.54±0.07
Topological invariant density χ [μm^{-3}]	7.23±0.00	-102.71±0.16	-117.36±1.15	-143.15±6.88	-7.43±0.51
Connectivity density c [μm^{-3}]	0.00±0.00	102.71±0.16	117.37±1.15	143.16±6.88	7.44±0.51

the shape factor density decreases (from 17.40 μm^{-2} to 7.82 μm^{-2} in 2D and 5.44 μm^{-2} in 3D).

The PE separator's shape factor density (6.68 μm^{-2}) is comparable to the ones of the datasets with straight pores in 2 and 3 directions, while the PP separator's shape factor density is lower (1.54 μm^{-2}) because of its higher proportion of concave regions at the pore surface.

4. Algorithm to generate artificial separator geometries

The following paragraph describes an algorithm to generate an artificial separator geometry consisting of solid elements and pore space. The pores are cylindrical and their orientation is always parallel to the IP1, IP2, or TP direction.

At first, a cuboid with desired dimensions is defined. In three different datasets, we create pores in the TP direction (1D pore directionality), pores parallel to the TP and IP1 direction (2D pore directionality), and pores parallel to the TP, IP1, and IP2 axis (3D pore directionality). The desired porosity of 40 % is divided by the number of pore directions (one, two, or three) in order to get the same porosity in all directions. The pore generating process consists of two major steps.

(i) On the face orthogonal to each desired pore direction, circles with a predefined radius (130 nm) are generated in an iterative manner. The number of circles is set by the porosity. The location of the circles is random with the only constraint that they cannot touch or intersect.

(ii) As soon as the necessary quantity of circles is created, they are extended through the entire separator producing the pores.

If more than one pore direction is wanted, the total porosity might be smaller than the addition of the directional porosities since pores may intersect. In this case, a new pore generating iteration is induced (starting from (i)) whereby the shortage in porosity is converted into the new number of circles to be created. This procedure runs until the target porosity of 40±2 % is met.

While the artificially generated 1D microstructures consist of individual pores that are not interconnected amongst each other, the artificially generated 2D and 3D microstructures are strongly interconnected and form a single connected pore network. This interconnectivity is not an implicit result of our algorithm for creating artificial microstructures, however, at 40 % porosity, it is extremely unlikely for cylindrical pores to penetrate 5 µm (= 500 voxels) thick structures without crossing another pore (probability ~ $(0.6)^{500}$). Therefore, none of the used artificially generated 2D and 3D microstructures contain isolated, non-interconnected pores.

Artificially generated 2D and 3D microstructures contain high fractions of third order nodes (see **Table III**). Nodes of order four (or higher) are only created if the central skeleton lines of two (or more) pores intersect in one single point. For pores of final diameter, such events have a low likelihood, and for most intersecting pores, the central skeleton lines of these pores will not intersect. Thus, several third order nodes are created instead of one single higher order node.

5. Shape analysis

For a 2D network, the connectivity C (number of loops) can be calculated via

$$C = N_B - N_N - N_{EP} + 1$$

with N_B being the number of branches, N_N being the number of nodes, and N_{EP} being the number of end points.[11] The description for connectivity using branches, end-points, and nodes is valid only in 2D; in 3D, the correct description uses edges, faces, and vertices of the single voxels.

For our structures with 1D and 2D pore directionality, the values for connectivity using the descriptions for 2D and 3D are the same. For the artificially generated pore structures in 3D and the recorded datasets, the values obtained via the 2D description are off by less than ±1 % compared to the values obtained via the 3D description.

6. Network analysis log-log-plots

In network theory, it is common to assess the node order distributions on a log-log plot. A Poisson distribution indicates a random network and power law distribution indicates a scale-free network.

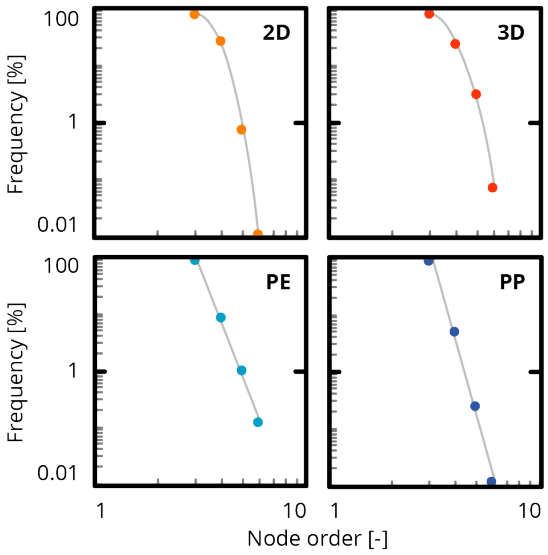

Figure S2. Log-log-plots of the node order distribution of the 2D and 3D reference datasets and the imaged PE and PP datasets.

Figure S2 shows that node order distribution in the 2D and 3D dataset follows an exponential distribution, while the distributions of the PE and PP datasets seem to follow a power law. However, to quantify the scaling of the node order, the distribution should exhibit a linear relationship on a log-log-plot over at least two orders of magnitude in both the x and y axes.[12] In standard processing of voxel-based data only nodes of order 3-6 can be reliably identified.[13] The x axis of **Figure S2**, therefore, spans less than one order of magnitude.

7. Pore orientation analysis

We determine the pore orientation angle distribution using ImageJ's *Directionality plugin* for the non-processed datasets for the PE (**Figure S3a**) and PP (**Figure S3b**) separators. As illustrated in the left-most images, the orientation angle is calculated for all pores in a plane, and each plane is indexed by the slice number in a specific direction (TP, IP1, or IP2). A vertical cut through any of the pore orientation angle distribution density plots (three plots to the right), would yield a histogram that represents the pore orientation distribution for that slice. For a slice (i.e., plane) with pores perpendicular to the slice, the orientation angle is 0°.

In the PE separator, for slices along the TP direction, the peak of the pore orientation distribution varies between 0° and 180°. This may be attributed to the presence of fibres in the IP direction located at different separator depths. For slices in the IP1 and IP2 directions, the pore orientation distributions are broadly and asymmetrically centred above 0°, indicating pores slanted at many different angles.

For PP, slices along the TP and IP1 are similar with orientation angle histograms centred around 90° due to its straight pore in the TP and IP1 directions.

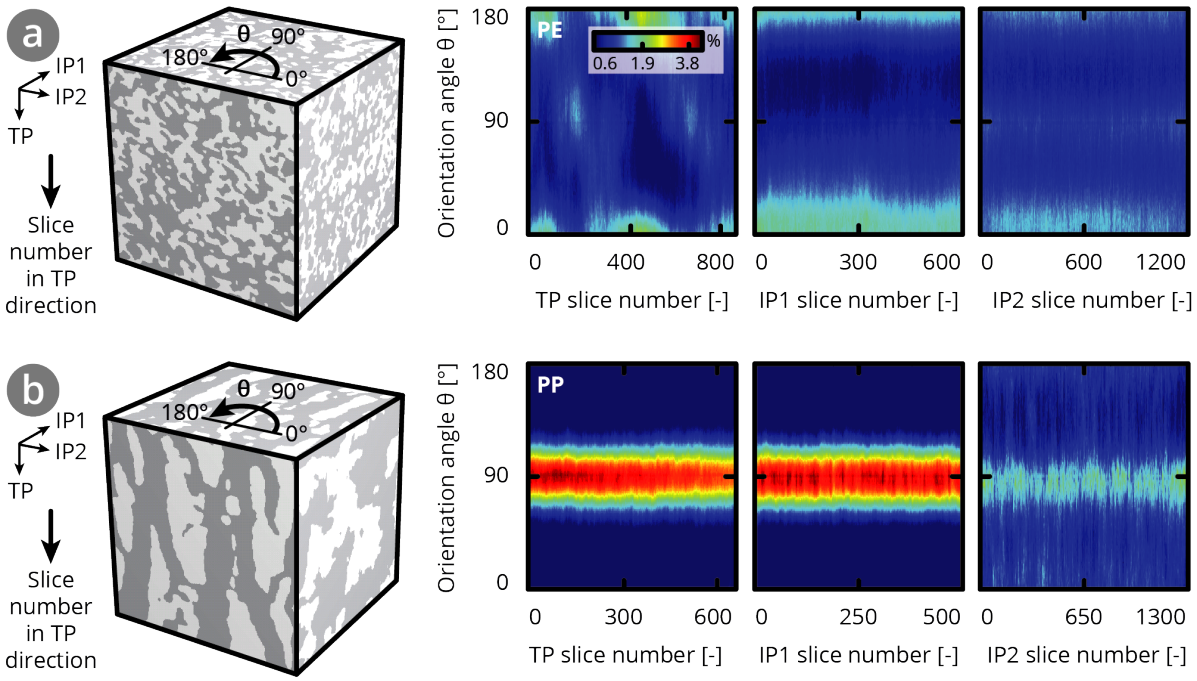

Figure S3. Orientation angle distributions across TP, IP1, and IP2 directions of the greyscale value, non-processed datasets of (a) Targray PE16A, and (b) Celgard® PP1615 separators.

8. End point analysis

The skeletonized pore space of the reference and imaged datasets of 5 µm edge length gives the total number of branches in the sub-volume, N_B. To obtain the number of network branches, N_n, we prune the skeletonized datasets using ImageJ's *AnalyseSkeleton 2D/3D plugin*. Subtracting the pruned skeleton from the original skeleton gives the number, $N_{EP*} = N_B - N_n$, of the end point branches within the volume and their coordinates. To account for end points that stem from cropping the datasets, we discard end point branches with coordinates within 5 voxels of the sub-volume's surface. We determine the end point density as the number of end point branches per volume (N_{EP*} / V), and the percentage of end point branches as the fraction of end point branches and the total number of branches (N_{EP*} / N_B).

9. Steady-state diffusion simulations

We simulate the C-rate dependence of the electrolyte salt concentration gradient across a Li^0|separator|LTO cell as shown in **Figure S4** and as described in our earlier work (Zahn *et al.*, DOI:10.1021/acsami.6b12085).[14] For detailed information about the simulation parameters (e.g., electrolyte properties, electrode properties) the reader is referred to the Supporting Information of this article.

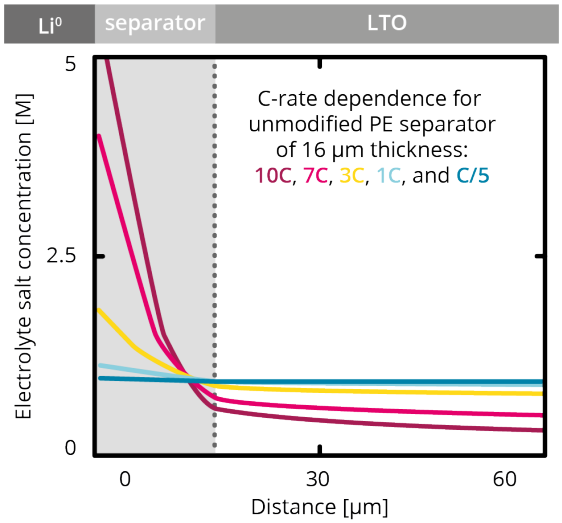

Figure S4. C-rate dependence of electrolyte salt concentration for Li^0|separator|LTO cells with Targray PE16A separator.

At 1C, a concentration difference of 0.25 M builds up across the 16 µm thick separator; this corresponds to a concentration difference of ~50 mM across a sub-volume of 3 µm edge length and to inlet and outlet concentrations of 1.25 and 1.20 M,

Table T2. Normalised Minkowski functionals m_0, m_1, m_2, as well as Euler-Poincaré characteristic and connectivity densities, χ and c, respectively, for a PP separator microstructure of edge length 3 µm as imaged, and with thin and broad nanofibers. The values for χ and c are calculated via the Minkowski functional M_3.

Datasets	PP1615	PP1615 with nanofibers of diameter 40 nm	PP1615 with nanofibers of diameter 60 nm
Porosity m_0 [%]	39.38	38.56	35.80
Specific surface area m_1 [µm^{-1}]	5.30	7.66	7.08
Shape factor density m_2 [µm^{-2}]	1.82	-3.31	-0.07
Topological invariant density χ [µm^{-3}]	-6.70	-94.07	-54.89
Connectivity density c [µm^{-3}]	6.74	94.11	54.93

respectively. We plot the broadening of the electrolyte salt concentration at each depth in the TP direction for artificially generated and imaged datasets (**Figure 4** in the main text). In the Supplementary Material of Ref. [15], we show the simulated ion concentration gradient in a graphite vs. NMC cell.

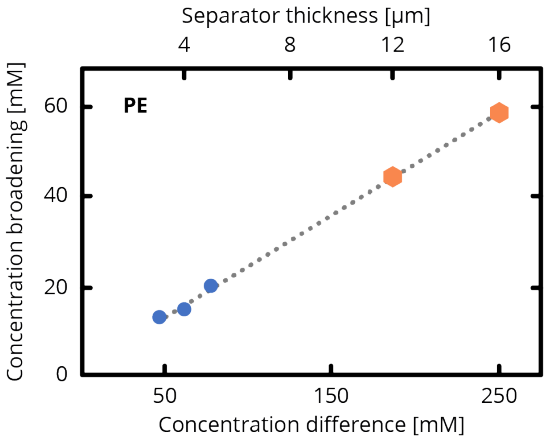

Figure S5. Calculated concentration broadening as function of sub-volume edge length of separator volume and corresponding concentration difference.

In **Figure S5**, we plot the concentration broadening (i.e., histogram width at half-depth of sub-volume) calculated for sub-volumes of 3, 4 and 5 µm (blue data points) against the concentration difference across a separator sub-volume (lower x-axis, range of values from **Figure S4**) and the edge length of the separator sub-volume (upper x-axis), and extrapolate the broadening of the electrolyte salt concentration to edge lengths of 12-16 µm (orange data points).

10. Adding nanofibers to Celgard® PP1615 separator geometries

Due to resolution limitations, the measured PP dataset does not feature the amorphous PP nanofibers spanning the large pore channels (partially visible in the SEM in **Figure 1b**). To assess how the presence of nanofibers in the large pore channels affects effective transport and topological properties of the separator geometry, cylindrical nanofibers with a diameter of 40 (thin nanofibers) and 60 nm (thick nanofibers) and distances of 50-70 nm are added to the pore channels of the recorded PP dataset. The diameter and the distances are estimated from FIB-SEM cross-sectional images.

At first, the existing separator geometry is loaded and rotated such that the direction along which the fibres have to be created corresponds to the IP2 axis. Then, the geometry is up-scaled isotropically in order to decrease voxel size followed by three-dimensional smoothing with a Gaussian kernel. Start points of a given number of fibres are randomly generated in the IP direction. The direction of each fibre is slightly deflected at random such that a direction distribution is created. A fibre ends as soon it (re-)enters the other side of the separator. All fibres are dilated to the desired radius and in a final step, the resulting structure is smoothed again.

11. Celgard® PP1615 separator geometries without and with nanofibers

Figure S6 shows that there is little difference between the calculated density plots for the electrolyte salt concentrations across a sub-volume of the PP1615 separator as imaged and with added nanofibers.

Thus, we conclude that – from a geometric perspective – the effective transport properties are not affected significantly by the presence of the PP nanofibers. The effect of the nanofibers cannot be neglected when modelling the mechanical properties of PP separators, as shown by Xu et al.[16] for Celgard® 2400 separator.

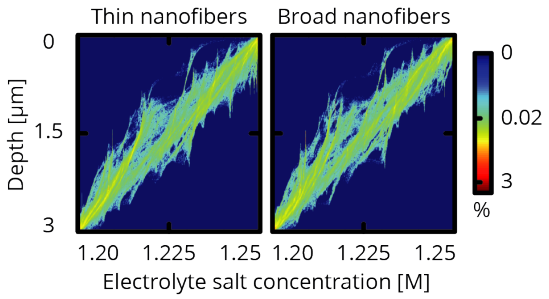

Figure S6. Electrolyte salt concentration across a sub-volume of 3 µm edge length of the Celgard® PP1615 separator dataset with artificially added thin (40 nm) and broad (60 nm) nanofibers.

The calculated Minkowski functional densities listed in **Table T2** show that adding nanofibers to the PP dataset results in a lower porosity, an increased specific surface area, a negative shape factor, and a more negative topological invariant. The latter corresponds to a more positive connectivity density (up to ~100 μm^{-3}), which is below the calculated connectivity density of PE. Since the surface integral of the mean curvature can be interpreted as the average of the mean curvature, a more positive shape factor indicates the presence of more convex parts. A negative shape factor like in the case of added nanofibers indicates thus more concave regions. For **Table T2**, we calculate the intensive Minkowski functionals for a single dataset of 3 µm edge length; in **Table II** in the main text, we calculate the average and standard deviation of the intensive Minkowski functionals for three datasets of 5 µm edge length.

References

1. Lagadec, M. F., Ebner, M., Zahn, R. & Wood, V. Communication - Technique for Visualization and Quantification of Lithium-Ion Battery Separator Microstructure. *J. Electrochem. Soc.* **163,** A992–A994 (2016).
2. Lagadec, M. F., Ebner, M. & Wood, V. Microstructure of Targray PE16A Lithium-Ion Battery Separator. (2016). doi:10.5905/ethz-1007-32
3. Lagadec, M. F. & Wood, V. Microstructure of Celgard® PP1615 Lithium-Ion Battery Separator. (2018). doi:10.3929/ethz-b-000265085
4. Vogel, H.-J., Weller, U. & Schlüter, S. Quantification of soil structure based on Minkowski functions. *Comput. Geosci.* **36,** 1236–1245 (2010).
5. Legland, D., Kiêu, K. & Devaux, M. F. Computation of Minkowski Measures on 2D and 3D Binary Images. *Image Anal Stereol* **26,** 83–92 (2007).
6. Mitra, P. P., Sen, P. N. & Schwartz, L. M. Short-time behavior of the diffusion coeffcient as a geometrical probe of porous media. *Phys. Rev. B* **47,** 8565–8574 (1993).
7. Strogatz, S. H. Exploring complex networks. *Nature* **410,** 268–276 (2001).
8. Zahn, R., Lagadec, M. F. & Wood, V. Transport in Lithium Ion Batteries: Reconciling Impedance and Structural Analysis. *ACS Energy Lett.* **2,** 2452–2453 (2017).
9. Ohser, J. & Mücklich, F. *Statistical Analysis of Microstructures in Materials Science*. (Wiley, 2000).
10. San José Martínez, F., Muñoz Ortega, F. J., Caniego Monreal, F. J., Kravchenko, A. N. & Wang, W. Soil aggregate geometry: Measurements and morphology. *Geoderma* **237–238,** 36–48 (2015).
11. Russ, J. C. *The Image Processing Handbook*. (CRC Press, Taylor & Francis Group, 2016).
12. Stumpf, M. P. H. & Porter, M. A. Critical Truths About Power Laws. *Science (80-.).* **335,** 665–666 (2012).
13. Reznikov, N. *et al.* Inter-trabecular angle: A parameter of trabecular bone architecture in the human proximal femur that reveals underlying topological motifs. *Acta Biomater.* **44,** 65–72 (2016).
14. Zahn, R., Lagadec, M. F., Hess, M. & Wood, V. Improving ionic conductivity and lithium-ion transference number in lithium-ion battery separators. *ACS Appl. Mater. Interfaces* **8,** 32637–32642 (2016).
15. Lagadec, M. F., Zahn, R. & Wood, V. Designing polyolefin separators to minimize the impact of local compressive stresses on lithium ion battery performance. *J. Electrochem. Soc.* **165,** A1829–A1836 (2018).
16. Xu, H., Zhu, M., Marcicki, J. & Yang, X. G. Mechanical modeling of battery separator based on microstructure image analysis and stochastic characterization. *J. Power Sources* **345,** 137–145 (2017).